Atmos. Meas. Tech. Discuss., doi:10.5194/amt-2016-133, 2016
Manuscript under review for journal Atmos. Meas. Tech.
Published: 27 April 2016
© Author(s) 2016. CC-BY 3.0 License.

Atmospheric Measurement Techniques
Open Access
Discussions

Accounting for the effects of surface BRDF on satellite cloud and trace-gas retrievals: A new approach based on geometry-dependent Lambertian-equivalent reflectivity applied to OMI algorithms

A. Vasilkov[1], W. Qin[1], N. Krotkov[2], L. Lamsal[3], R. Spurr[4], D. Haffner[1], J. Joiner[2], E.-S. Yang[1], and S. Marchenko[1]

[1]Science Systems and Applications Inc., Lanham, MD, USA
[2]NASA Goddard Space Flight Center, Greenbelt, MD, USA
[3]Universities Space Research Association, Columbia, MD, USA
[4]RT Solutions, Cambridge, MA, USA

Correspondence to: A. Vasilkov
(alexander.vasilkov@ssaihq.com)

Abstract. Most satellite nadir ultraviolet and visible cloud, aerosol, and trace-gas algorithms make use of climatological surface reflectivity databases. For example, cloud and NO_2 retrievals for the Ozone Monitoring Instrument (OMI) use monthly gridded surface reflectivity climatologies that do not depend upon the observation geometry. In reality, reflection of incoming direct and diffuse solar light from land or ocean surfaces is sensitive to the sun-sensor geometry. This dependence is described by the bidirectional reflectance distribution function (BRDF). To account for the BRDF, we propose to use a new concept of geometry-dependent Lambertian-equivalent reflectivity (LER). Implementation within the existing OMI cloud and NO_2 retrieval infrastructure requires changes only to the input surface reflectivity database. The geometry-dependent LER is calculated using a vector radiative transfer model with high spatial resolution BRDF information from the MODerate-resolution Imaging Spectroradiometer (MODIS) over land and the Cox-Munk slope distribution over ocean with a contribution from water-leaving radiance. We compare the geometry-dependent and climatological LERs for two wavelengths, 354 and 466 nm, that are used in OMI cloud algorithms to derive cloud fractions. A detailed comparison of the cloud fractions and pressures derived with climatological and geometry-dependent LERs is carried out. Geometry-dependent LER and corresponding retrieved cloud products are then used as inputs to our OMI NO_2 algorithm. We find that the use of high-resolution geometry-dependent LERs can increase NO_2 vertical columns by up to 50% in highly polluted areas.

Atmos. Meas. Tech. Discuss., doi:10.5194/amt-2016-133, 2016
Manuscript under review for journal Atmos. Meas. Tech.
Published: 27 April 2016
© Author(s) 2016. CC-BY 3.0 License.

1 Introduction

Satellite ultraviolet and visible (UV/Vis) nadir backscattered sunlight trace-gas, aerosol, and cloud retrieval algorithms must accurately estimate the reflection by the Earth's surface in order to produce high quality data sets. Surface reflectivity climatologies used in most current algorithms are typically gridded monthly Lambertian-equivalent reflectivities (LERs) that have been derived from satellite observations (e.g., Herman and Celarier, 1997; Kleipool et al., 2008; Russell et al., 2011). These climatologies generally have no dependence on the observation geometry. However, it is well known that both ocean and land reflectivity depend upon viewing and illumination geometry. This dependence is described by the bidirectional reflectance distribution function (BRDF), mathematically expressed as

$$\mathrm{BRDF}(\omega_i,\omega_r) = \frac{dI(\omega_r)}{I(\omega_i)cos(\theta_i)d\omega_i}, \quad (1)$$

where $dI(\omega_r)$ is the portion of total radiance reflected in the direction defined by the vector ω_r due to the illuminating irradiance, F, from the direction defined by the vector ω_i: $dF(\omega_i) = I(\omega_i)cos(\theta_i)d\omega_i$, θ_i is the angle between the normal to the surface and the direction of illuminating light, and $d\omega_i$ is the element of the solid angle (Nicodemus, 1965; Schaepman-Strub et al., 2006; Martonchik et al., 2000). When the surface is illuminated by a parallel beam of light, the integral over the solid angle of reflected light

$$\mathrm{BSA}(\omega_i) = \int \mathrm{BRDF}(\omega_r,\omega_i)\cos(\theta_r)d\omega_r \quad (2)$$

provides the so-called Black Sky Albedo (BSA) of the surface. It follows from Eq. 2 that the BRDF of a perfect Lambertian surface is equal to $1/\pi$.

The frequently used dimensionless bidirectional reflectance factor (BRF) is defined as "the ratio of the radiant flux reflected by a sample surface to the radiant flux reflected into the identical beam geometry by an ideal (lossless) and diffuse (Lambertian) standard surface, irradiated under the same conditions as the sample surface" (Schaepman-Strub et al., 2006). In general, the relationship between BRF and BRDF for an arbitrary surface can be obtained from Eq. 1 by using BRDF=$1/\pi$ for an ideal Lambertian surface, i.e.,

$$\mathrm{BRF}(\omega_i,\omega_r) = dI(\omega_i,\omega_r)/dI_{Lam}(\omega_i) = \pi\mathrm{BRDF}(\omega_i,\omega_r). \quad (3)$$

BRF and BRDF are both inherent properties of the surface that do not depend on the illumination conditions (Schaepman-Strub et al., 2006). While BRDF is a function describing a surface for all possible illuminating and reflected directions, the BRF refers to a specific illumination and observational geometry for a given measurement. BRF from satellite observations can therefore differ significantly for the same area over different days owing to variations in sun-satellite geometries. In other words, for a given surface BRDF is always the same (neglecting seasonal changes), but BRF changes from day to day depending on observational conditions.

Atmos. Meas. Tech. Discuss., doi:10.5194/amt-2016-133, 2016
Manuscript under review for journal Atmos. Meas. Tech.
Published: 27 April 2016
© Author(s) 2016. CC-BY 3.0 License.

Many satellite UV/Vis algorithms are based on the so-called mixed Lambert-equivalent reflectivity (MLER) model, first introduced by Seftor et al. (1994). For example, the MLER concept is currently used in most trace gas (Boersma et al., 2011; Bucsela et al., 2013) and cloud (Acarreta et al., 2004; Joiner and Vasilkov, 2006) retrieval algorithms for the Ozone Monitoring Instrument (OMI), a Dutch/Finnish UV/Vis sensor (Levelt et al., 2006) flying on the NASA Aura satellite. The MLER model treats cloud and ground as horizontally homogeneous Lambertian surfaces and mixes them using the independent pixel approximation (IPA). According to the IPA, the measured top-of-atmosphere (TOA) radiance is a sum of the clear sky and overcast subpixel radiances that are weighted with an effective cloud fraction (ECF). The ECF is calculated by inverting

$$I_m = I_g(R_g)(1 - \mathrm{ECF}) + I_c(R_c)\mathrm{ECF} \quad (4)$$

at a wavelength not substantially affected by rotational-Raman scattering (RRS) or atmospheric absorption, where I_m is the measured TOA radiance, I_g and I_c are the precomputed clear sky (ground) and overcast (cloudy) subpixel radiances, R_g and R_c and the corresponding ground and cloud Lambertian-equivalent reflectivities (LERs), respectively.

The MLER model typically assumes $R_c = 0.8$. This value of R_c was used by McPeters et al. (1996) for a UV total column O_3 algorithm and independently derived by Koelemeijer et al. (2001) for use in near-infrared O_2 A-band cloud pressure retrievals. The assumption of $R_c = 0.8$ effectively accounts for Rayleigh scattering in partially cloudy scenes (Ahmad et al., 2004). This approach also accounts for scattering/absorption that occurs below a thin cloud.

The MLER model compensates for photon transport within a cloud by placing the Lambertian surface somewhere in the middle of the cloud instead of at the top (Vasilkov et al., 2008). As clouds are vertically inhomogeneous, the pressure of this surface does not necessarily correspond to the geometrical center of the cloud, but rather to the so-called optical centroid pressure (OCP) (Vasilkov et al., 2008; Joiner et al., 2012). The cloud OCP can be thought of and modeled as a reflectance-averaged pressure level reached by back-scattered photons (Joiner et al., 2012). Cloud OCPs are the appropriate quantity for use in trace-gas retrievals from similar instruments (Vasilkov et al., 2004; Joiner et al., 2006, 2009).

In one of the few studies to explore the effects of surface BRDF on satellite trace gas retrievals, Zhou et al. (2010) show how various treatments of surface reflectance, including BRDF, affect OMI tropospheric NO_2 retrievals over Europe. Their study, which covers the months of July and November, suggested that account of surface BRDF effects can change NO_2 retrievals by up to 20% with the largest effects at high view angles. Ignoring the surface BRDF can also introduce NO_2 retrieval errors that vary with land type (Noguchi et al., 2014). In an effort to improve NO_2 retrievals over China, Lin et al. (2014, 2015) revised the calculation of tropospheric air mass factor (AMF) in the Dutch OMI NO_2 (DOMINO) product using improved information for cloud, aerosols, and BRDF from the MODerate-resolution Imaging Spectroradiometer (MODIS); they reported better agreement with independent NO_2 observations. Our motivations for this work follow from these studies

Atmos. Meas. Tech. Discuss., doi:10.5194/amt-2016-133, 2016
Manuscript under review for journal Atmos. Meas. Tech.
Published: 27 April 2016
© Author(s) 2016. CC-BY 3.0 License.

Atmospheric Measurement Techniques Discussions
Open Access

that offered valuable insights into the effects of the surface BRDF on NO_2 retrievals. We continue in this line of investigation by (1) examining in detail the BRDF effect on retrieved cloud parameters that are important inputs for trace-gas retrievals including NO_2; (2) additionally investigating BRDF impact on cloud and NO_2 retrievals over ocean; and (3) providing a computationally efficient method of accounting for BRDF effects that can be incorporated into existing retrieval algorithms with minimal changes.

To account for surface BRDF, we introduce the concept of a geometry-dependent surface LER. The geometry-dependent LER is derived from TOA radiance computed with Rayleigh scattering and BRDF for the particular geometry of a satellite-based pixel. This approach does not require any major changes to existing MLER trace gas and cloud algorithms. The main revision to the algorithms requires replacement of the existing static LER climatologies with LERs calculated for specific field-of-view (FOV) sun-satellite geometries. The geometry-dependent surface LER approach can be applied to any current and future satellite algorithms that use the MLER concept.

We implement the geometry-dependent LERs based on a MODIS BRDF product and use these LERs within OMI cloud and NO_2 algorithms. It should be noted that the MODIS BRDF product is derived from the atmospherically corrected TOA reflectances (i.e., aerosol and Rayleigh scattering effects are removed at the high spatial resolution of MODIS). In contrast, the climatological LERs currently used in OMI algorithms, from either the Total Ozone Mapping Spectrometer (TOMS) or OMI, are derived by correcting only for Rayleigh scattering and thus include aerosol effects (see details in Herman and Celarier, 1997; Kleipool et al., 2008). Therefore, the use of the geometry-dependent LER product in trace gas algorithms over heavily polluted regions may also require an explicit account of aerosols (Lin et al., 2015). In this study we do not consider aerosol effects.

2 Satellite data sets and radiative transfer model

2.1 VLIDORT code

For all radiative transfer (RT) calculations, we use the Vector Linearized Discrete Ordinate Radiative Transfer (VLIDORT) code (Spurr, 2006). VLIDORT computes the Stokes vector in a plane-parallel atmosphere with a non-Lambertian underlying surface. It has the ability to deal with attenuation of solar and line-of-sight paths in a spherical atmosphere, which is important for large solar zenith angles (SZA) and viewing zenith angles (VZA). Unlike Lin et al. (2014, 2015), we use a vector code because neglect of polarization can lead to considerable errors for modeling backscatter spectra in UV/Vis. This is particularly the case for modeling backscatter spectra over the ocean where reflection of unpolarized light from the flat ocean surface at the Brewster angle leads to its perfect linear polarization (Vasilkov et al., 1990a,b).

Atmos. Meas. Tech. Discuss., doi:10.5194/amt-2016-133, 2016
Manuscript under review for journal Atmos. Meas. Tech.
Published: 27 April 2016
© Author(s) 2016. CC-BY 3.0 License.
Atmospheric Measurement Techniques Discussions

2.2 MODIS BRDF data set

We use the MODIS gap-filled BRDF Collection 5 product MCD43GF (Schaaf et al., 2002, 2011). This product provides three coefficients, a_i, as a function of time and spatial coordinates for three BRDF kernels: 1) isotropic, $k_{iso} \equiv 1$; 2) volumetric, k_{vol}; and 3) geometric, k_{geo}. The BRDF coefficients are dynamic, i.e., 16-day averages for every 8 days of the year from 2003 to present. They are provided for snow-free land and permanent ice at a high spatial resolution (30 arc sec). In this study we do not consider temporary snow-covered areas. In principal, those areas can be treated with the approach of McLinden et al. (2014) that is based on the MODIS-derived albedo product. Unlike Lin et al. (2015), we do not use MODIS data over coastal zones and inland waters, because the MODIS kernel model is not applicable for water surfaces. Instead of MODIS data, we apply our ocean model described in Section 3 to the coastal zones and inland waters.

2.3 OMI data sets

2.3.1 OMI cloud algorithms

In this paper, we examine the BRDF effects on two OMI cloud algorithms, one based on rotational-Raman scattering (RRS) in the UV and the other on O_2-O_2 absorption at 477 nm. The O_2-O_2 cloud algorithm developed by the authors and used here is similar to an operational O_2-O_2 cloud algorithm developed at the Royal Meteorological Institute of the Netherlands (KNMI), known as OMCLDO2, (Acarreta et al., 2004; Sneep et al., 2008), but differs in a few respects described below.

Both the RRS and O_2-O_2 algorithms utilize the MLER concept. We use 354 and 466 nm in the RRS O_2-O_2 algorithms, respectively, to compute ECF. It should be noted that the ECF implicitly accounts for non-absorbing aerosols, treating them as clouds and this increases cloud fraction.

The OMI RRS cloud algorithm is detailed in Joiner et al. (2004), Joiner and Vasilkov (2006), and Vasilkov et al. (2008). OCP is derived from the high-frequency structure in the TOA reflectance caused by RRS in the atmosphere. The OCP is retrieved by a minimum-variance technique that spectrally fits the observed TOA reflectance within the spectral window of 345.5–354.5 nm. The RRS algorithm does not report the cloud OCP for ECF< 0.05 owing to large retrieval errors at small values of ECF (Vasilkov et al., 2008).

Our O_2-O_2 cloud algorithm retrieves OCP from OMI-derived oxygen dimer slant column densities (SCD) at 477 nm. Our algorithm spectral fitting differs from KNMI's in that it utilizes temperature-dependent O_2-O_2 cross-sections (Thalman and Volkamer, 2013) and incorporates a new fitting technique similar to that developed by Marchenko et al. (2015) for NO_2 SCD retrieval. The fitting procedure derives the O_2-O_2 SCD using retrieved O_3 and NO_2 slant column estimates from independent OMI algorithms.

The OCP is estimated using the MLER method to compute the appropriate air mass factors (AMF)

Atmos. Meas. Tech. Discuss., doi:10.5194/amt-2016-133, 2016
Manuscript under review for journal Atmos. Meas. Tech.
Published: 27 April 2016
© Author(s) 2016. CC-BY 3.0 License.

Atmospheric Measurement Techniques Discussions

(Yang et al., 2015). To solve for OCP, we invert

$$\mathrm{SCD} = \mathrm{AMF}_g(P_s, R_g)\mathrm{VCD}(P_s)(1 - f_r) + \mathrm{AMF}_c(\mathrm{OCP}, R_c)\mathrm{VCD}(\mathrm{OCP})f_r, \quad (5)$$

where VCD is the vertical column density (VCD=SCD/AMF), AMF_g and AMF_c are the precomputed (at 477 nm) clear sky (ground) and overcast (cloudy) subpixel AMFs, P_s is the surface pressure, and f_r is the cloud radiance fraction (CRF) given by $f_r = \mathrm{ECF} * I_c/I_m$. Lookup tables of the TOA radiances and AMFs were generated using VLIDORT. Temperature profiles needed for computation of VCD and AMF are taken from the Global Modeling Initiative (GMI) chemistry transport model (Strahan et al., 2007) driven by the NASA GEOS-5 global data assimilation system (Rienecker et al., 2011). Comparisons of the retrieved OCPs with those from the operational KNMI OMI O_2-O_2 algorithm, OMCLDO2, have shown good agreement with a correlation coefficient of ∼0.99 for ECF> 0.2 when identical surface climatological LERs are used.

2.3.2 OMI NO_2 algorithm

The OMI NO_2 spectral fitting algorithm (OMNO2A) currently uses differential optical absorption spectroscopy (DOAS) to fit OMI-measured spectra in the wavelength range 405–465 nm to estimate total (stratospheric and tropospheric) NO_2 SCDs (Boersma et al., 2011). The SCDs are then converted to NO_2 VCDs using pre-calculated AMFs: VCD=SCD/AMF using the algorithm known as OMNO2B (Bucsela et al., 2013; Lamsal et al., 2014). For fixed (measured) SCD, the retrieved NO_2 VCD is inversely proportional to the AMF.

3 Basic approach

The BRDF over land is calculated as $\mathrm{BRDF} = a_{iso} + a_{vol}k_{vol} + a_{geo}k_{geo}$, where the coefficients $a_{iso}, a_{vol}, a_{geo}$ come from MODIS data, the volumetric kernel, k_{vol} describes light reflection from a dense leaf canopy, and the geometric kernel,k_{geo} describes light reflection from a sparse ensemble of surface objects casting shadows on the background assumed to be Lambertian. The kernels are the only angle-dependent functions, which expressions are given in Lucht et a. (2000). The BRDF coefficients are spatially averaged over an actual satellite FOV and used to calculate TOA radiance for its observation geometry.

The BRDF coefficients depend on wavelength. For the present study we selected two wavelengths in the UV and Vis: 354 and 466 nm. These wavelengths are relatively free of atmospheric rotational Raman scattering (RRS) and trace gas absorption. The BRDF coefficients at 466 nm are directly taken from the MCD43GF product at 470 nm that is provided at a spatial resolution of 30 arc sec (Schaaf et al., 2002, 2011). Because the MODIS product is not available at 354 nm, we adjusted the 470 nm LERs to account for potential spectral dependences. The adjustment applies the spectral ratio of climatological OMI-derived LERs: $R(354)/R(470)$ similar to the approach of McLinden et

Atmos. Meas. Tech. Discuss., doi:10.5194/amt-2016-133, 2016
Manuscript under review for journal Atmos. Meas. Tech.
Published: 27 April 2016
© Author(s) 2016. CC-BY 3.0 License.

Atmospheric Measurement Techniques Discussions

al. (2014). Using climatological data of Kleipool et al. (2008) we find that this ratio is close to unity (within $\pm 5\%$) for most areas.

To calculate TOA radiance over water surfaces, we account for both light specularly reflected from a rough water surface and diffuse light backscattered by water bulk and transmitted through the water surface. We neglect contributions from oceanic foam. Reflection from the water surface is described by the Cox-Munk slope distribution function (Cox and Munk, 1954). We use an isotropic form of the Cox-Munk distribution in which the facet-slope variance is independent of wind direction. All computations use a wind speed of 5 m/s which is close to the climatological mean.

Diffuse light from the ocean is described by a Case 1 water model that has chlorophyll concentration as a single input parameter (Morel, 1988). Our Case 1 water model accounts for the anisotropic nature of light backscattered by the ocean (Morel and Gentili, 1996). A spatial distribution of chlorophyll concentration is taken from the monthly SeaWiFS climatology. The common Case 1 water model developed for the Vis (Morel, 1988) was extended to the UV using data from Vasilkov et al. (2002, 2005). To calculate water-leaving radiance, we need to know the downwelling atmospheric transmittance at the surface. The transmittance is obtained by calculating the total atmospheric direct and diffuse downwelling flux at the surface. The diffuse contribution in the transmittance will itself depend on the water-leaving radiance. To calculate the atmospheric transmittance, we introduce in VLIDORT a module for the iterative calculation of the transmittance, in which the first computation is made for a dark surface, and this is then used again as input to the water-leaving contribution. This process is repeated until convergence of the transmittance is achieved (3 or 4 iterations are sufficient).

To estimate LER over over mixed surface types, we compute an area-weighted radiance for uniform land and water contributions within an OMI FOV. The LER for heterogeneous surface pixels is then calculated from this linear combination of radiances. The high spatial resolution MYD43GF product supplies an eight category land water classification map at the same resolution as the BRDF parameters. We convert this map into a binary land-water mask by merging all shorelines and ephemeral water into the land category and classifying all other water sub-categories simply as water. We then compute the areal fraction of land and water for each OMI FOV. For specification of the OMI pixel, we used the OMPIXCOR product that provides coordinates of OMI pixel corners (http://disc.sci.gsfc.nasa.gov/uui/datasets/OMPIXCOR_V003/summary). We used an option of overlapping pixels in the along track direction corresponding to 75% energy in the along-track FOV. In this option the edges of the FOV are aligned in the cross track direction but overlap in the along track direction.

Given the computed TOA radiance, I_{TOA}, the LER is calculated by inverting

$$I_{TOA}(\lambda,\theta,\theta_0,\phi,P_s,R) = I_0(\lambda,\theta,\theta_0,\phi,P_s) + \frac{RT(\lambda,\theta,\theta_0,P_s)}{1-RS_b(\lambda,P_s)}, \tag{6}$$

where λ is wavelength, θ is the VZA, θ_0 is the SZA, ϕ is the relative azimuth angle, R is the LER, I_0 is the TOA radiance calculated for a black surface, T is the quantity representing the total trans-

Atmos. Meas. Tech. Discuss., doi:10.5194/amt-2016-133, 2016
Manuscript under review for journal Atmos. Meas. Tech.
Published: 27 April 2016
© Author(s) 2016. CC-BY 3.0 License.

Atmospheric Measurement Techniques
Discussions

mittance in the viewing direction when the atmosphere is illuminated from below by a Lambertian reflection of all energy incident upon the ground, and S_b is the diffuse flux reflectivity of the atmosphere for the case of its isotropic illumination from below (Chandrasekhar, 1960; Dave, 1978). To speed up computations, we created lookup tables of the quantities I_0, T, and S_b for selected wavelengths.

4 Geometry-dependent LER

Because reflection of incoming solar light from non-Lambertian surfaces depends on satellite observational geometry, the same area observed at different geometries can have different LERs. Figure 1 shows the MODIS-based high spatial resolution LER over the US Baltimore-Washington corridor for two consecutive days (Jan. 17 and 18, 2005) computed using the OMI observational geometry. The SZA and VZA values are in the similar ranges for both days. However, there is a large difference in the relative azimuth angle which varies from around 63° for Jan. 17 to about 118° for Jan. 18. Since the land tends to have strong backward scattering, that explains the higher LER for Jan. 18 than that for Jan. 17. The differences, if not accounted for, may produce errors in the trace gas retrievals.

A comparison of the computed geometry-dependent and climatological LERs at 466 nm is shown in Fig. 2 for OMI orbit 12414 on 13 Nov 2006. The climatological LERs (monthly) are derived from OMI observations (Kleipool et al., 2008). In general, the eastern portion of the orbital swath (that has a later equator crossing time) has higher values of the LERs than the western part. This is an effect of the OMI observational geometry and BRDF increase in the backscattered direction.

Figure 2 shows significant differences between the geometry-dependent and climatological LERs for both land and ocean. Over land, the climatological LERs are mostly higher than the geometry-dependent LERs. This is presumably because the geometry-dependent LERs are derived from atmospherically corrected MODIS radiances while the climatological LERs are affected by residual aerosols. Moreover, climatological LERs are inherently contaminated by clouds owing to substantially larger sizes of OMI pixels as compared with those of MODIS. This is particularly true for the Amazonia region where clouds are persistent.

Over ocean, the geometry-dependent LERs are systematically higher than the climatological LERs in areas affected by sun glint and at large VZAs. This is because the climatological LERs are based on the mode of LERs from a long time series of observations over a given area; this minimizes the impact of observations affected by sun glint and high values that occur at large VZAs.

Figure 3 shows the geometry-dependent LERs computed at 466 and 354 nm and their differences for same OMI orbit 12414. Here, we assume that the BRDF coefficients over land are spectrally independent. The LER differences over land are thus solely due to the smoothing effect of enhanced Rayleigh scattering in UV that increases the diffuse to direct incident irradiance ratio as compared

Atmos. Meas. Tech. Discuss., doi:10.5194/amt-2016-133, 2016
Manuscript under review for journal Atmos. Meas. Tech.
Published: 27 April 2016
© Author(s) 2016. CC-BY 3.0 License.

Atmospheric Measurement Techniques Discussions

with 466 nm. Over land, LER(354) $<$ LER(466), but the differences are relatively small (< 0.015).

Over the ocean, the LER differences additionally result from the spectral dependence of water-leaving radiance. Over the sunglint areas, the solar light reflected from the ocean surface is significantly brighter at 466 nm than at 354 nm thus leading to higher LERs. Over areas less affected by sunglint, LER(354) $>$ LER(466) in general owing to higher amounts of water leaving radiance.

It is interesting to note that the patterns of rivers and their tributaries are evident in the LER maps of Fig. 3 for both 354 and 466 nm. This effect is most pronounced when rivers are viewed from the OMI measurement geometry that registers the reflectance signal of Fresnel reflection from smooth river surfaces. It may be somewhat surprising that this appears at OMI spatial resolution; we can explain the effect by considering that while the LER from FOVs comprised of river areas and surrounding land is weighted linearly by the areal fraction of each, reflectance from the river surface is disproportionally high owing to the Fresnel reflection in sun-glint geometry. Outside of the regions where OMI observes glint, the LER in the Amazon basin may still be higher than expected owing to the turbidity of some rivers in the Amazon floodplain that varies seasonally.

5 BRDF effects on the OMI cloud products

5.1 RRS algorithm

Figure 4 shows ECFs computed with geometry-dependent LERs and the differences with respect to the climatological LERs (ΔECF). The largest ΔECFs (up to 0.05) take place over the less cloudy Amazonian areas. ΔECF is obviously lower for cloudy areas owing to the diminished effect of surface properties on TOA radiance. The heavily cloudy areas are easily identified on the ΔECF map.

We next examine the most interesting range of ECF for trace-gas retrievals, ECF < 0.25, which corresponds to $f_r <$ 0.4–0.5. For this range, Figure 5 shows a scatter plot of the ECFs retrieved with the geometry-dependent versus climatological LERs and how ΔECF varies with ECF. Only data from 50°S to 50°N are used in Fig. 5 and all subsequent similar figures. This latitude range excludes areas with snow for which MODIS BRDF data are not available. On average, ΔECF is small and positive for the ocean (~ 0.02). Over land ΔECF is even lower and ranges from ∼-0.01 to ∼0.015 for ECF< 0.25. The standard deviation of ΔECF does not depend much on ECF. It is ∼0.01 over ocean and ∼0.015 over land. Even though ΔECF is small on average, it can be as large as ± 0.05 which is quite substantial for the low ECF range.

Figure 6 similarly shows OCPs retrieved with the geometry-dependent LER and the differences with respect to those retrieved using the climatological LERs (ΔOCP) for OMI orbit 12414. There are no obvious geographical patterns in the ΔOCP map. ΔOCP can be as large as ± 100 hPa. The OCP differences are particularly pronounced along the edges of cloud systems. Spatial correlation between ΔOCP (Fig. 6) and ΔECF (Fig. 4) is not apparent. As may be expected, ΔOCP decreases

Atmos. Meas. Tech. Discuss., doi:10.5194/amt-2016-133, 2016
Manuscript under review for journal Atmos. Meas. Tech.
Published: 27 April 2016
© Author(s) 2016. CC-BY 3.0 License.

with increasing ECF. Figure 7 is similar to Fig. 5 but for OCP. On average, ΔOCP is small (∼ 10.0 hPa) with standard deviation of up to ∼40 hPa.

5.2 O_2-O_2 algorithm

Here we show similar comparisons of the cloud products retrieved with the geometry-dependent and climatological LERs for ECF<0.25. Figure 8 is similar to Fig. 5 but for ECF from the O_2-O_2 algorithm. ΔECF <∼0.03 over land and <∼0.01 over ocean.

Figure 9 is similar to Fig. 7 but for OCP from the O_2-O_2 algorithm. ΔOCP has values up to 200 hPa. The mean ΔOCPs are significantly larger for the O_2-O_2 algorithm as compared with RRS. On average, ΔOCP varies from ∼80 hPa at ECF=0.05 to 5 hPa at ECF = 0.25 over land. ΔOCP is noticeably lower over ocean. The standard deviation, up to 100 hPa, is also higher than that from the RRS cloud algorithm. This can be explained by decreasing Rayleigh optical thickness at 477 nm, which results in a larger fraction of direct solar irradiance illuminating the surface and larger BRDF effects.

6 BRDF effects on the OMI NO_2 retrievals

We consider the BRDF effect on the NO_2 AMFs only, because the retrieved NO_2 amount is inversely proportional to the AMF. The tropospheric NO_2 AMF, $\mathrm{AMF_{trop}}$, is calculated using the MLER model with input cloud parameters from the O_2-O_2 algorithm assuming *a priori* NO_2 vertical profile shapes (see Fig. 10):

$$\mathrm{AMF_{trop}} = \mathrm{AMF}_g(P_s, R_g)(1-f_r) + \mathrm{AMF}_c(\mathrm{OCP}, R_c) f_r. \quad (7)$$

The effect of a surface reflectivity change, ΔR_g, of 0.01 on AMF_g is shown as a function of R_g in Fig. 10. The Jacobian, $J = \Delta\mathrm{AMF}_g/\Delta R_g$, is always positive because larger surface reflectances increase satellite sensitivity to NO_2 absorption in the lowest atmosphere. J decreases with increasing R_g and for unpolluted NO_2 mixing ratios (Fig. 10).

The BRDF effect on AMF_g for OMI observational geometries and ground resolution can be estimated from Figures 2 and 10 using $\Delta R_g = \mathrm{LER(BRDF)} - \mathrm{LER}$. The effect is largest over polluted regions in the eastern US, where ΔR_g is negative with values –0.03 to –0.02 (Fig. 2), LER ~ 0.05 and $\Delta\mathrm{AMF}_g$ ∼ –20% to –30%. The BRDF effect reverses over water for glint geometries and large viewing angles, but R_g is large here and the effect on AMF_g is reduced (i.e., small Jacobian).

To estimate the BRDF effect on $\mathrm{AMF_{trop}}$ we need to account for the f_r change as well:

$$\Delta\mathrm{AMF_{trop}} = \Delta\mathrm{AMF}_g(R_g)(1-f_r) + \Delta f_r[\mathrm{AMF}_c(\mathrm{OCP}, R_c) - \mathrm{AMF}_g(R_g)]. \quad (8)$$

The cloud AMF strongly depends on the OCP, since high clouds (low OCP) have a shielding effect and low clouds (high OCP), aerosols, and fog can enhance AMF_c. Assuming a negligible NO_2

Atmos. Meas. Tech. Discuss., doi:10.5194/amt-2016-133, 2016
Manuscript under review for journal Atmos. Meas. Tech.
Published: 27 April 2016
© Author(s) 2016. CC-BY 3.0 License.

mixing ratio above the cloud OCP, we can neglect AMF_c and Eq. 8 simplifies to

$$\Delta\mathrm{AMF}_{\mathrm{trop}} = \Delta\mathrm{AMF}_g(R_g)(1-f_r) - \Delta f_r \mathrm{AMF}_g(R_g) \quad (9)$$

Over land, BRDF reduces the geometry-dependent LER as compared with the LER climatology, (i.e., $\Delta R_g < 0$) leading to smaller values of AMF_g (Fig. 10). At the same time, the mean ECF increases by 0.02 (Fig. 8) and this produces even larger increases in f_r ($\Delta f_r \sim 0.04$). Therefore both terms in the above equation are negative meaning that switching to a geometry-dependent LER reduces $\mathrm{AMF}_{\mathrm{trop}}$ even more over land. The effect is mixed over water, since both ΔR_g or Δf_r can change signs for certain geometries.

Figure 11 shows that the calculated BRDF impact on $\mathrm{AMF}_{\mathrm{trop}}$ arising from both surface BRDF and O_2-O_2 cloud parameters exhibits a strong spatial variation with smaller effects over ocean, unpolluted, or cloudy areas. Over land, where the geometry-dependent LER is generally lower than the climatological LER, use of the BRDF data results in lower AMFs and higher tropospheric NO_2 VCDs. The effect is enhanced over polluted areas such as eastern US, where the changes in AMF can reach up to 50%. The effect is reduced for unpolluted and overcast conditions and mixed over oceans, because R_g increases for sunglint and large VZA directions but decreases for other directions.

Figure 12 compares the clear-sky $\mathrm{AMF}_{\mathrm{trop}}$ calculated using climatological and geometry-dependent LERs. The use of geometry-dependent LERs generally leads to lower $\mathrm{AMF}_{\mathrm{trop}}$ by up to 29% over land and 15% over ocean. Differences in O_2-O_2 cloud parameters resulting from the use of geometry-dependent LERs add additional scatter, changing $\mathrm{AMF}_{\mathrm{trop}}$ by -42–5% over land and -22–13% over ocean. $\mathrm{AMF}_{\mathrm{trop}}$ differences are large for low AMFs, driven by enhanced differences in LER, OCP, or f_r.

Figure 13 illustrates how the use of geometry-dependent LER changes NO_2 retrievals over clean and polluted areas. Consistent with previous studies by Lin et al. (2014, 2015), AMFs are considerably lower with geometry-dependent LERs. This suggests that the current operational NO_2 products based on climatological LERs could be underestimated by up to 48% over China. The eastern US exhibits similar but somewhat smaller differences. Minor changes are expected over unpolluted and overcast areas.

7 Conclusions

We developed a new concept of geometry-dependent surface LER and provided a means for computing it. Spatially averaged high-resolution MODIS BRDFs are used for computation of the geometry-dependent LER over land for OMI pixels. The Cox-Munk slope distribution function and the Case 1 water-leaving radiance model are utilized for computation of the geometry dependent LER over ocean. This method accounts for the geometrical dependence of LER within the existing framework of MLER trace gas and cloud algorithms with only minimal changes. It is important to note

© Author(s) 2016. CC-BY 3.0 License.

that the geometry-dependent surface LER approach can be applied to any current or future satellite algorithms that utilize MLER trace gas and cloud algorithms.

We examined the effects of the geometry-dependent LER on OMI cloud and NO_2 algorithms. The effects on retrieved cloud parameters were relatively small on average and diminish with increasing cloud fraction. Even though the impact is small on average, it can be as large as ± 0.05 for the effective cloud fraction and 100 hPa for the cloud optical centroid pressure. The BRDF effects were noticeably higher for the O_2-O_2 algorithm that uses visible wavelengths as compared with the RRS algorithm that utilizes a UV spectral range. This can be explained by the stronger smoothing effect of Rayleigh scattering in the UV as compared with the Vis.

We also find that the use of geometry-dependent LER increases the OMI NO_2 vertical columns by up to 50% over highly polluted areas. Only minor changes to NO_2 columns (within 5%) are found over unpolluted and overcast areas.

In the future, we plan to implement the use of geometry-dependent LERs in our cloud and NO_2 OMI algorithms. Along with the use of the geometry-dependent LER product, we plan to explicitly include aerosols in the NO_2 algorithm. Further evaluation of the results with OMI data is ongoing. We also plan to investigate the use a new surface BRDF product from the multi-angle implementation of atmospheric correction (MAIAC) algorithm (Lyapustin et al., 2012).

Acknowledgements. Funding for this work was provided in part by the NASA through the Aura science team program. We thank P. K. Bhartia for helpful discussions, Z. Ahmad for providing data for comparisons, A. Sayer for provision of an updated ocean optics model used in the water-leaving supplement of the VLIDORT code, and C. B. Schaaf for consultation on the use of the MODIS BRDF product.

Atmos. Meas. Tech. Discuss., doi:10.5194/amt-2016-133, 2016
Manuscript under review for journal Atmos. Meas. Tech.
Published: 27 April 2016
© Author(s) 2016. CC-BY 3.0 License.

References

Acarreta, J. R., De Haan, J. F., and Stammes, P.: Cloud pressure retrieval using the O_2-O_2 absorption band at 477 nm, J. Geophys. Res.-Atmos., 109, D05204, doi:10.1029/2003jd003915, 2004.

Ahmad, Z., Bhartia, P. K., and Krotkov, N.: Spectral properties of backscattered UV radiation in cloudy atmospheres, J. Geophys. Res., 109, D01201, doi:10.1029/2003JD003395, 2004.

Boersma, K. F., Eskes, H. J., Dirksen, R. J., van der A, R. J., Veefkind, J. P., Stammes, P., Huijnen, V., Kleipool, Q. L., Sneep, M., Claas, J., Leitão J., Richter, A., Zhou, Y., and Brunner, D.: An improved tropospheric NO_2 column retrieval algorithm for the Ozone Monitoring Instrument, Atmos. Meas. Tech., 4, 1905–1928, doi:10.5194/amt-4-1905-2011, 2011.

Bucsela, E. J., Krotkov, N. A., Celarier, E. A., Lamsal, L. N., Swartz, W. H., Bhartia, P. K., Boersma, K. F., Veefkind, J. P., Gleason, J. F., and Pickering, K. E.: A new stratospheric and tropospheric NO_2 retrieval algorithm for nadir-viewing satellite instruments: applications to OMI, Atmos. Meas. Tech., 6, 2607–2626, doi:10.5194/amt-6-2607-2013, 2013.

Radiative Transfer, Dover Publications, Inc., N.Y., 1960, (see Eq. 200).

Cox, C. and Munk, W.: Statistics of the sea surface derived from sun glitter, J. Mar. Res. 13, 198–227, 1954.

Dave, J. V.: Effect of aerosol on the estimation of total ozone in an atmospheric column from the measurements of the ultraviolet radiance, J. Atmos. Sci., 35, 899–911, 1978.

Herman, J. R. and Celarier, E.: Earth surface reflectivity climatology at 340 to 380 nm from TOMS data, J. Geophys. Res. 102, 28003–28011, 1997.

Joiner, J., Vasilkov, A. P., Flittner, D. E., Gleason, J. F., and Bhartia, P. K.: Retrieval of cloud chlorophyll content using Raman scattering in GOME spectra, J. Geophys. Res., 109, D01109, doi:10.1029/2003JD003698, 2004.

Joiner J. and Vasilkov, A.P.: First Results from the OMI Rotational-Raman Scattering Cloud Pressure Algorithm, IEEE Trans. Geophys. Remote Sens., 44, 1272–1282, 2006.

Joiner, J., Vasilkov, A. P., Yang, K., and Bhartia, P. K.: Observations over hurricanes from the ozone monitoring instrument, Geophys. Res. Lett., 33, L06807, doi:10.1029/2005GL025592, 2006.

Joiner, J., Schoeberl, M. R., Vasilkov, A. P., Oreopoulos, L., Platnick, S., Livesey, N. J., and Levelt, P. F.: Accurate satellite-derived estimates of the tropospheric ozone impact on the global radiation budget, Atmos. Chem. Phys., 9, 4447–4465, 2009.

Joiner, J. Vasilkov, A. P., Gupta, P., Bhartia, P. K.,Veefkind, P., Sneep, M., de Haan, J., Polonsky, I., and Spurr, R.: Fast simulators for satellite cloud optical centroid pressure retrievals; evaluation of OMI cloud retrievals, Atmos. Meas. Tech., 5, 529–545, doi:10.5194/amt-5-529-2012, 2012.

Kleipool, Q. L., Dobber, M. R., de Haan, J. F., and Levelt, P. F.: Earth surface reflectance climatology from 3 years of OMI data, J. Geophys. Res., 113, D18308, doi:10.1029/2008jd010290, 2008.

Koelemeijer, R. B. A., Stammes, P., Hovenier, J. W., and de Haan, J. F.: A fast method for retrieval of cloud parameters using oxygen A-band measurements from the Global Ozone Monitoring Experiment, J. Geophys. Res., 106, 3475–3496, 2001.

Lamsal, L. N., Krotkov, N. A., Celarier, E. A., Swartz, W. H., Pickering, K. E., Bucsela, E. J., Gleason, J. F., Martin, R. V., Philip, S., Irie, H., Cede, A., Herman, J., Weinheimer, A., Szykman, J. J., and Knepp, T. N.: Evaluation of OMI operational standard NO_2 column retrievals using in situ and surface-based NO_2

© Author(s) 2016. CC-BY 3.0 License.

observations, Atmos. Chem. Phys., 14, 11587-11609, doi:10.5194/acp-14-11587-2014, 2014.

Levelt, P. F., van der Oord, G. H. J., Dobber, M. R., Malkki, A., Visser, H., de Vries, J., Stammes, P., Lundell, J. O. V., and Saari, H.: The ozone monitoring instrument, IEEE T. Geosci. Remote, 44, 1093–1101, 2006.

Lin, J.-T., Martin, R. V., Boersma, K. F., Sneep, M., Stammes, P., Spurr, R., Wang, P., Van Roozendael, M., Clémer, K., and Irie, H.: Retrieving tropospheric nitrogen dioxide from the Ozone Monitoring Instrument: effects of aerosols, surface reflectance anisotropy, and vertical profile of nitrogen dioxide, Atmos. Chem. Phys., 14, 1441–1461, doi:10.5194/acp-14-1441-2014, 2014.

Lin, J.-T., Liu, M.-Y., Xin, J.-Y., Boersma, K. F., Spurr, R., Martin, R., and Zhang, Q.: Influence of aerosols and surface reflectance on satellite NO_2 retrieval: seasonal and spatial characteristics and implications for NO_x emission constraints, Atmos. Chem. Phys., 15, 11217–11241, doi:10.5194/acp-15-11217-2015, 2015.

An algorithm for the retrieval of albedo from space using semiempirical BRDF models, IEEE T. Geosci. Remote, 38, 977–998, 2000.

Lyapustin, A., Wang, Y., Laszlo, I., Hilker, T., Hall, F., Sellers, P., Tucker, J., Korkin, S.: Multi-angle implementation of atmospheric correction for MODIS (MAIAC). 3: Atmospheric correction, Rem. Sens. Environ., http://dx.doi.org/10.1016/j.rse.2012.09.002, 2012.

Marchenko, S., Krotkov, N. A., Lamsal, L. N., Celarier, E. A., Swartz, W. H., and Bucsela, E. J.: Revising the slant column density retrieval of nitrogen dioxide observed by the Ozone Monitoring Instrument, J. Geophys. Res., 120, 5670–5692, 2015.

Martonchik, J. V., Bruegge, C. J., and Strahler, A. H.: A review of reflectance nomenclature used in remote sensing, Remote Sens. Reviews, 19, 9–20, 2000.

McLinden, C.A., Fioletov, V., Boersma, K. F., Kharol, S. K., Krotkov, N., Lamsal, L., Makar, P. A., Martin, R. V., Veefkind, J. P., and Yang, K.: Improved satellite retrievals of NO_2 and SO_2 over the Canadian oil sands and comparisons with surface measurements, Atmos. Chem. Phys., 14, 3637–3656, doi:10.5194/acp-14-3637-2014, 2015.

Morel, A.: Optical modeling of the upper ocean in relation to its biogeneous matter content (Case I waters), J. Geophys. Res., 93, 10749–10768, 1988.

Morel, A. and Gentili, B.: Didduse reflectance of oceanic water. III. Implication of bidirectionality for the remote-sensing probe, Appl. Opt., 35, 4850–4862, 1996.

Noguchi, K., Richter, A., Rozanov, V., Rozanov, A., Burrows, J. P., Irie, H., and Kita, K.: Effect of surface BRDF of various land cover types on geostationary observations of tropospheric NO_2, Atmos. Meas. Tech., 7, 3497-3508, doi:10.5194/amt-7-3497-2014, 2014.

Nicodemus, F.: Directional reflectance and emissivity of an opaque surface, Appl. Opt., 4, 767-775, 1965.

McPeters, R., Bhartia, P. K., Krueger, A. J., Herman, J. R., Schlesinger B. M., Wellemeyer, C. G., Seftor, C. J., Jaross G., Taylor S. L., Swissler T., Torres, O., Labow, G., Byerly W., and Cebula R. P.: Nimbus-7 Total Ozone Mapping Spectrometer (TOMS) data products user′s guide, NASA Reference Publication 1384, 1996.

Rienecker, M. M., Suarez, M. J., Gelaro, R., Todling, R., Bacmeister, J., Liu, E., Bosilovich, M. G., Schubert, S. D., Takacs, L., Kim, G.-K., Bloom, S., Chen, J., Collins, D., Conaty, A., da Silva, A., Gu, W., Joiner, J., Koster, R. D., Lucchesi, R., Molod, A., Owens, T., Pawson, S., Pegion, P., Redder, C. R., Reichle, R., Robertson, F. R., Ruddick, A. G., Sienkiewicz, M., and Woollen, J.: MERRA: NASA′s Modern-Era Retrospective Analysis for Research and Applications, J. Climate, 24, 3624?3648, doi:10.1175/JCLI-D-11-

00015.1, 2011.

Russell, A. R., Perring, A. E., Valin, L. C., Bucsela, E. J., Browne, E. C., Wooldridge, P. J., and Cohen, R. C.: A high spatial resolution retrieval of NO_2 column densities from OMI: method and evaluation, Atmos. Chem. Phys., 11, 8543–8554, doi:10.5194/acp-11-8543–2011, 2011.

Schaaf, C. B., Gao, F., Strahler, A. H., Lucht, W., Li, X., Tsang, T., Strugnell, N. C., Zhang, X., Jin, Y., Muller, J.-P., Lewis, P., Barnsley, M., Hobson, P., Disney, M., Roberts, G., Dunderdale, M., Doll, C., d'Entremont, R., Hu, B., Liang, S., and Privette, J. L.: First operational BRDF, albedo and nadir reflectance products from MODIS, Remote Sens. Environ., 83, 135–148, 2002.

Schaaf, C. L. B., Liu, J., Gao, F., and Strahler, A. H.: MODIS albedo and reflectance anisotropy products from Aqua and Terra, In Land Remote Sensing and Global Environmental Change: NASA's Earth Observing System and the Science of ASTER and MODIS, Remote Sensing and Digital Image Processing Series, Vol.11, B. Ramachandran, C. Justice, M. Abrams, Eds, Springer-Verlag, 873 pp., 2011.

Schaepman-Strub, G., Schaepman, M. E., Painter, T. H., Dangel, S., Martonchik, J. V., Reflectance quantities in optical remote sensing–definitions and case studies, Remote Sens. Environ., 103, 27–42, 2006.

Seftor, C. J., Taylor, S. L., Wellemeyer, C. G., and McPeters, R. D.: Effect of Partially-Clouded Scenes on the Determination of Ozone, Ozone in the Troposphere and Stratosphere, Part 1, Proceedings of the Quadrennial Ozone Symposium, Charlottesville, USA, 1992, NASA Conference Publication 3266, 919-922, 1994.

Sneep, M., de Haan, J., Stammes, P., Wang, P., Vanbauce, C., Joiner, J., Vasilkov, A. P., and Levelt, P. F.: Three way comparison between OMI/Aura and POLDER/PARASOL cloud pressure products, J. Geophys. Res., 113, D15S23, doi:10.1029/2007JD008694, 2008.

Spurr, R. J. D.: VLIDORT: a linearized pseudo-spherical vector discrete ordinate radiative transfer code for forward model and retrieval studies in multilayer multiple scattering media, J. Quant. Spectr. Rad. Trans., 102, 316–421, 2006.

Stammes, P., Sneep, M., de Haan, J. F., Veefkind, J. P., Wang, P., and Levelt, P. F.: Effective cloud fractions from the Ozone Monitoring Instrument: Theoretical framework and validation, J. Geophys. Res., 113, D16S38, doi:10.1029/2007JD008820, 2008.

Strahan, S. E., Duncan, B. N., and Hoor, P.: Observationally derived transport diagnostics for the lowermost stratosphere and their application to the GMI chemistry and transport model, Atmos. Chem. Phys., 7, 2435–2445, doi:10.5194/acp-7-2435-2007, 2007.

Thalman, R., and Volkamer, R.: Temperature dependent absorption cross-sections of O_2-O_2 collision pairs between 340 and 630 nm and at atmospherically relevant pressure, Phys. Chem. Chem. Phys., 15, 2013.

Vasilkov, A. P., Kondranin, T. V., Krotkov, N. A., Lakhtanov, G. A., Churov, V. E.: Properties of the angular dependence of polarization for upward radiation from the sea surface in the visible region of the spectrum, Izvestiya, Atmosph. Oceanic Phys., 26, 397–401, 1990.

Vasilkov, A. P., Kondranin, T. V., Krotkov, N. A.: The effectiveness of polarization measurements in passive remote sensing of the ocean in the visible region of the spectrum, Sov. J. Remote Sensing, 7, 886–899, 1990.

Vasilkov, A. P., Herman, J., Krotkov, N. A., Kahru, M., Mitchell, B. G., and Hsu, C.: Problems in assessment of the UV penetration into natural waters from space-based measurements, Opt. Eng., 41, 3019–3027, 2002.

Vasilkov, A. P., Joiner, J., Yang, K., and Bhartia, P. K.: Improving total column ozone retrievals by using cloud pressures derived from Raman scattering in the UV, Geophys. Res. Lett., 31, L20109,

© Author(s) 2016. CC-BY 3.0 License.

doi:10.1029/2004GL020603, 2004.

Vasilkov, A.P., Herman, J., Ahmad, Z., Kahru, M., Mitchell, B. G.: Assessment of the ultraviolet radiation field in ocean waters from space-based measurements and full radiative-transfer calculations, Appl. Opt., 44, 2863–2869, 2005.

Vasilkov, A. P., Joiner, J., Spurr, R., Bhartia, P. K., Levelt, P. F., and Stephens, G.: Evaluation of the OMI cloud pressures derived from rotational Raman scattering by comparisons with other satellite data and radiative transfer simulations, J. Geophys. Res., 113, D15S19, doi:10.1029/2007JD008689, 2008.

Yang, E.-S., Vasilkov, A., Joiner, J., Marchenko, S., Krotkov, N., Haffner, D., and Bhartia, P. K.: A new cloud pressure algorithm based on the O_2-O_2 absorption band at 477 nm, OMI Science Team Meeting, de Bilt, Netherlands, 2015. Available at http://projects.knmi.nl/omi/research/project/meetings/ostm19/pres_ostm19_20150831.php.

Zhou, Y., Brunner, D., Spurr, R. J. D., Boersma, K. F., Sneep, M., Popp, C., and Buchmann, B.: Accounting for surface reflectance anisotropy in satellite retrievals of tropospheric NO_2, Atmos. Meas. Tech., 3, 1185–1203, doi:10.5194/amt-3-1185- 2010, 2010.

Atmos. Meas. Tech. Discuss., doi:10.5194/amt-2016-133, 2016
Manuscript under review for journal Atmos. Meas. Tech.
Published: 27 April 2016
© Author(s) 2016. CC-BY 3.0 License.

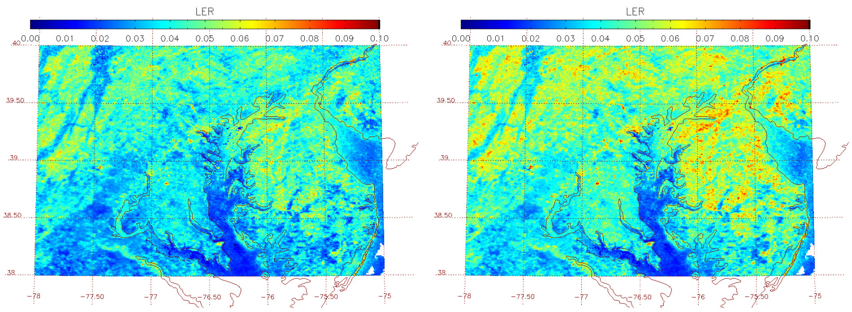

Fig. 1. High spatial resolution MODIS-based LERs for the Baltimore-Washington corridor for 17 (left) and 18 (right) Jan. 2005 computed for OMI observational geometries.

Atmos. Meas. Tech. Discuss., doi:10.5194/amt-2016-133, 2016
Manuscript under review for journal Atmos. Meas. Tech.
Published: 27 April 2016
© Author(s) 2016. CC-BY 3.0 License.

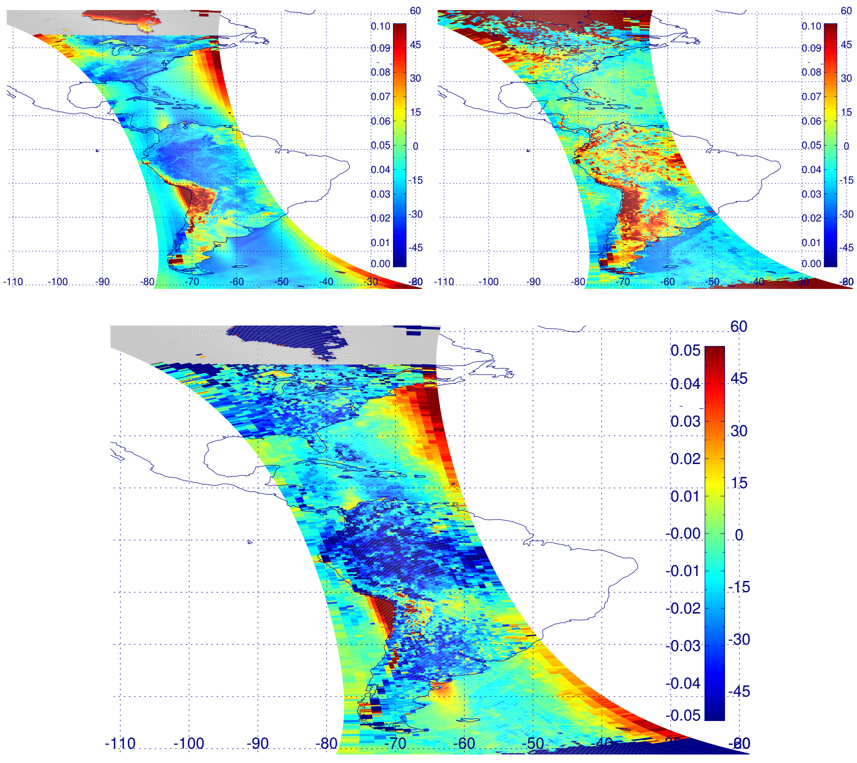

Fig. 2. LERs computed at 466 nm for OMI orbit 12414 on 13 Nov. 2006 using MODIS-based BRDF with OMI geometry (upper left), OMI-based monthly climatology (upper right), and their difference (MODIS-based minus climatological LERs, lower panel) Missing MODIS BRDF data are shown in grey here and elsewhere.

© Author(s) 2016. CC-BY 3.0 License.

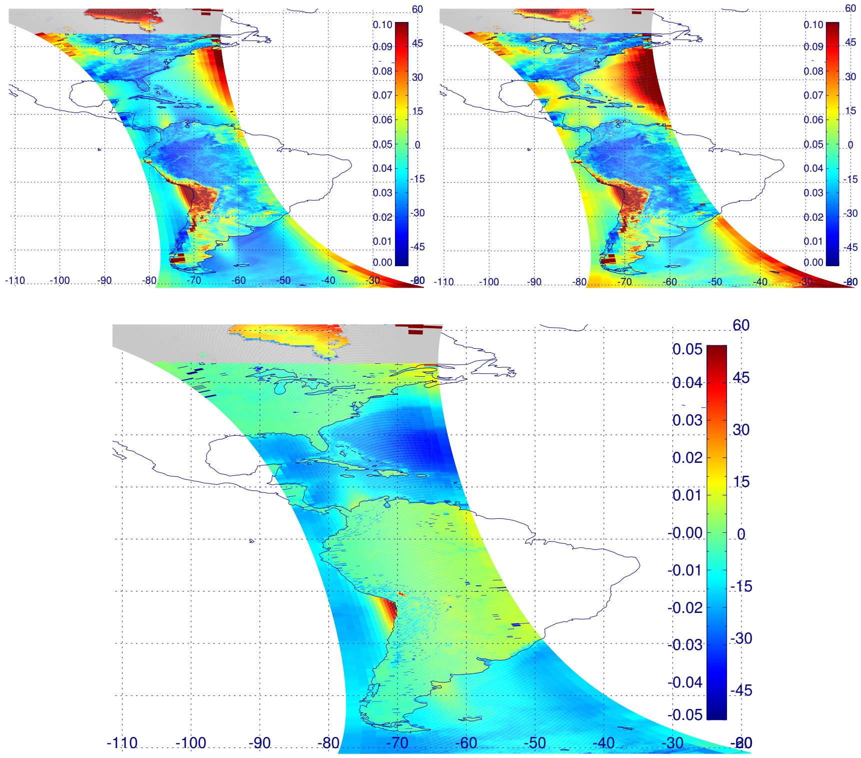

Fig. 3. Similar to Fig. 2 but showing geometry-dependent LERs computed for 466 nm (upper left), 354 nm (upper right), and their difference (466 nm minus 354 nm LER, lower panel).

Atmos. Meas. Tech. Discuss., doi:10.5194/amt-2016-133, 2016
Manuscript under review for journal Atmos. Meas. Tech.
Published: 27 April 2016
© Author(s) 2016. CC-BY 3.0 License.

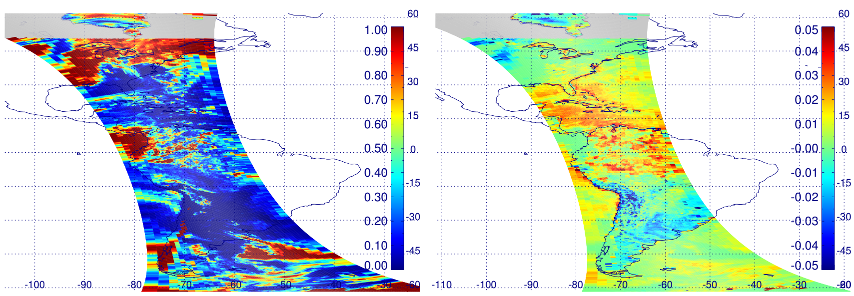

Fig. 4. RRS-derived ECF computed with geometry-dependent LERs (left) and the difference between the ECFs computed with geometry-dependent and climatological LERs (right).

Atmos. Meas. Tech. Discuss., doi:10.5194/amt-2016-133, 2016
Manuscript under review for journal Atmos. Meas. Tech.
Published: 27 April 2016
© Author(s) 2016. CC-BY 3.0 License.

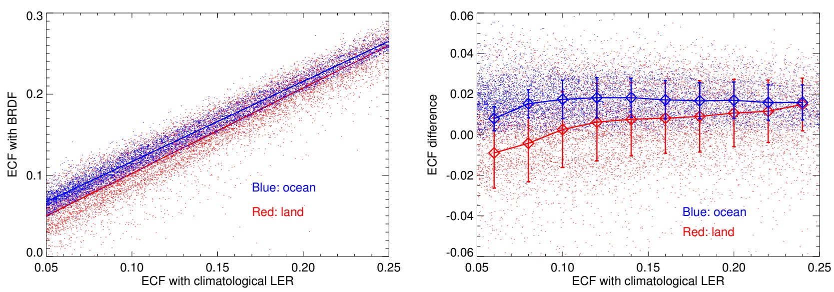

Fig. 5. Scatter plot of RRS-retrieved effective cloud fractions (ECFs) computed with geometry-dependent LERs versus climatological LERs for ECF< 0.25 with linear fits (left), and the mean ECF difference (diamonds) and standard deviation (error bars) as a function of ECF (right).

Atmos. Meas. Tech. Discuss., doi:10.5194/amt-2016-133, 2016
Manuscript under review for journal Atmos. Meas. Tech.
Published: 27 April 2016
© Author(s) 2016. CC-BY 3.0 License.

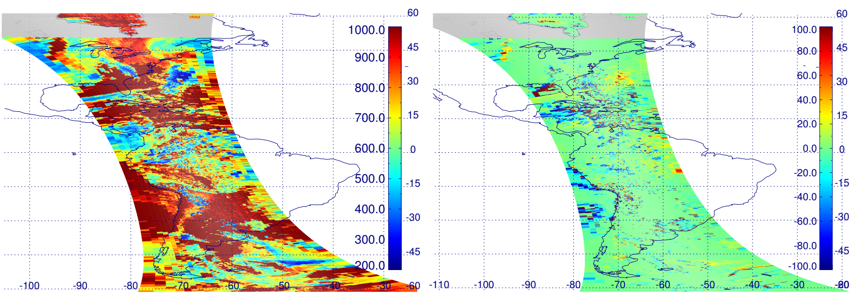

Fig. 6. RRS-retrieved cloud optical centroid pressure (OCP) computed with geometry-dependent LERs (left) and the difference between the OCPs computed with geometry-dependent and climatological LERs (right).

Atmos. Meas. Tech. Discuss., doi:10.5194/amt-2016-133, 2016
Manuscript under review for journal Atmos. Meas. Tech.
Published: 27 April 2016
© Author(s) 2016. CC-BY 3.0 License.

Atmospheric Measurement Techniques Discussions

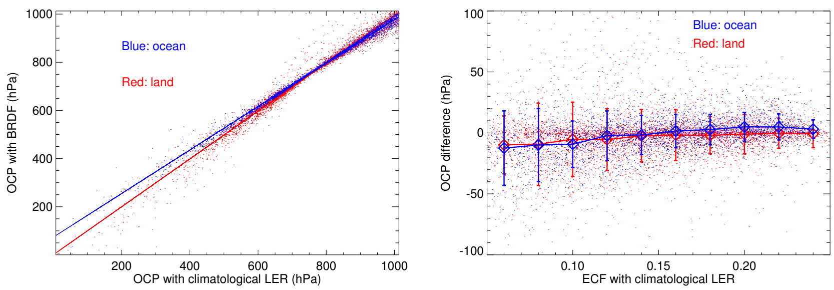

Fig. 7. Similar to Fig. 5 but for cloud optical centroid pressures (OCP).

Atmos. Meas. Tech. Discuss., doi:10.5194/amt-2016-133, 2016
Manuscript under review for journal Atmos. Meas. Tech.
Published: 27 April 2016
© Author(s) 2016. CC-BY 3.0 License.

Atmospheric Measurement Techniques Discussions

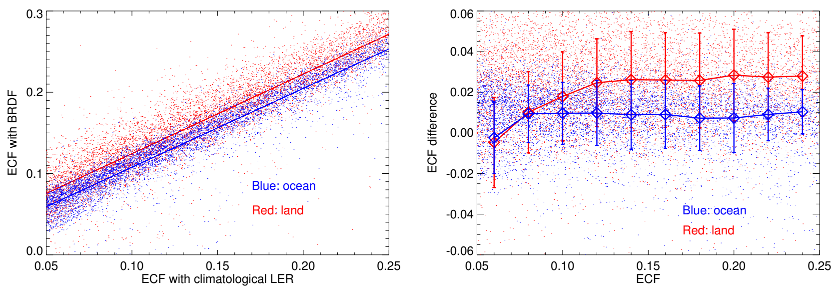

Fig. 8. Similar to Fig. 5 but for effective cloud fraction (ECF) from the O_2-O_2 algorithm.

Atmos. Meas. Tech. Discuss., doi:10.5194/amt-2016-133, 2016
Manuscript under review for journal Atmos. Meas. Tech.
Published: 27 April 2016
© Author(s) 2016. CC-BY 3.0 License.

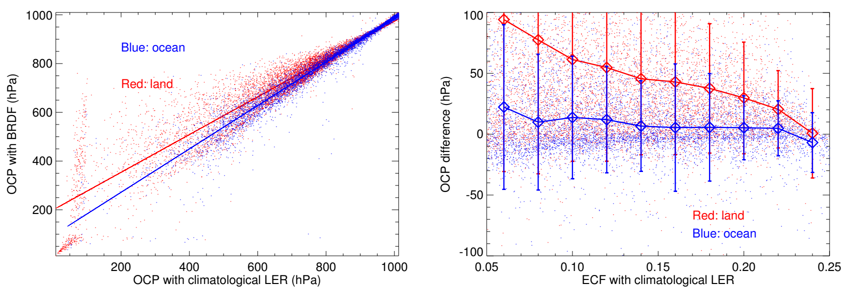

Fig. 9. Similar to Fig. 7 but for cloud optical centroid pressure (OCP) from the O_2-O_2 algorithm.

Atmos. Meas. Tech. Discuss., doi:10.5194/amt-2016-133, 2016
Manuscript under review for journal Atmos. Meas. Tech.
Published: 27 April 2016
© Author(s) 2016. CC-BY 3.0 License.

Atmospheric Measurement Techniques Discussions

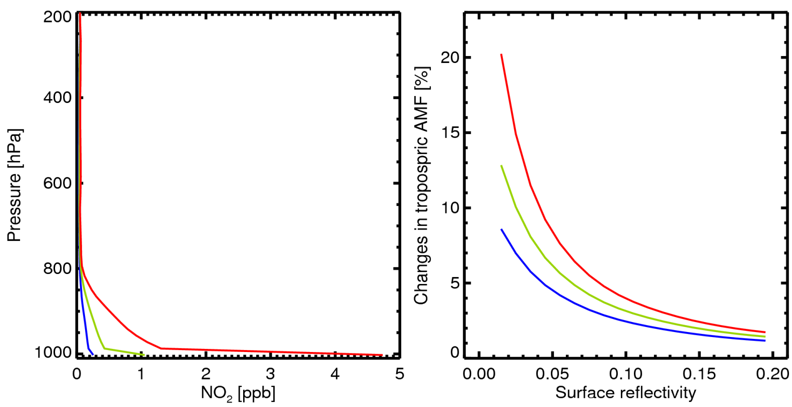

Fig. 10. June mean NO_2 profiles at three locations in the eastern US from the NASA GMI model (left) and air mass factor (AMF) change due to 0.01 change in reflectivity as a function of surface reflectivity (right); Red: highly polluted profile, green: moderately polluted, blue: unpolluted profile.

Atmos. Meas. Tech. Discuss., doi:10.5194/amt-2016-133, 2016
Manuscript under review for journal Atmos. Meas. Tech.
Published: 27 April 2016
© Author(s) 2016. CC-BY 3.0 License.

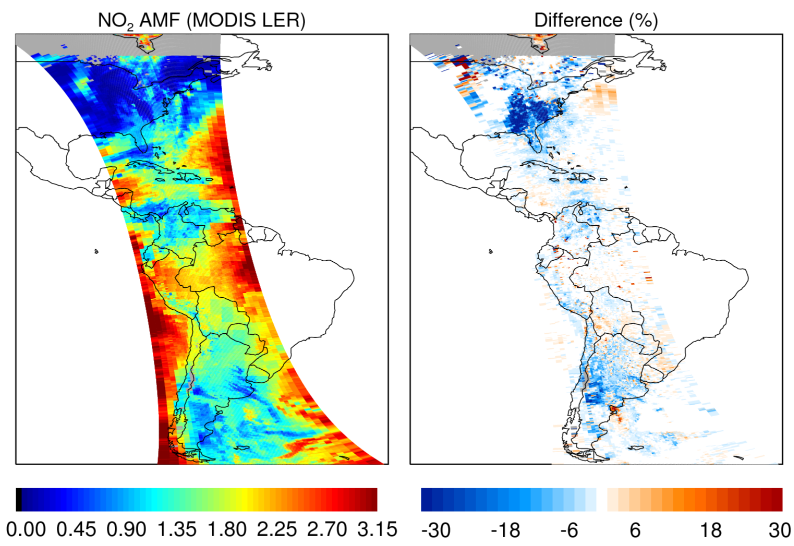

Fig. 11. OMI tropospheric NO_2 air mass factor (AMF) calculated using geometry-dependent MODIS-based LER (left) and percent differences with respect to climatological LERs (right).

Atmos. Meas. Tech. Discuss., doi:10.5194/amt-2016-133, 2016
Manuscript under review for journal Atmos. Meas. Tech.
Published: 27 April 2016
© Author(s) 2016. CC-BY 3.0 License.

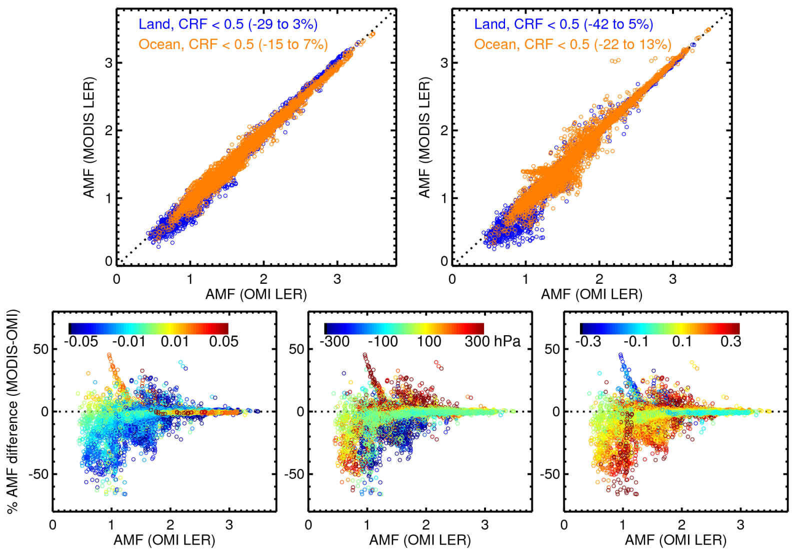

Fig. 12. Top panels: Scatter diagrams of AMFs calculated using geometric-dependent MODIS-based LER versus OMI-based climatological LER for the orbit 12414 for clear to moderately cloudy sky ($f_r < 0.5$) including effects of BRDF only (clouds unchanged, left) and the effects of both BRDF and O_2-O_2 cloud parameters (right) for land (blue) and ocean (orange). Numbers in parentheses represent % difference at the 2nd and 98th percentile range. Bottom panels: % difference in AMF with changes in surface BRDF and O_2-O_2 cloud parameters, sorting the data by the difference with respect to LER (left), OCP (middle), and f_r (right).

Atmos. Meas. Tech. Discuss., doi:10.5194/amt-2016-133, 2016
Manuscript under review for journal Atmos. Meas. Tech.
Published: 27 April 2016
© Author(s) 2016. CC-BY 3.0 License.

Atmospheric Measurement Techniques Discussions

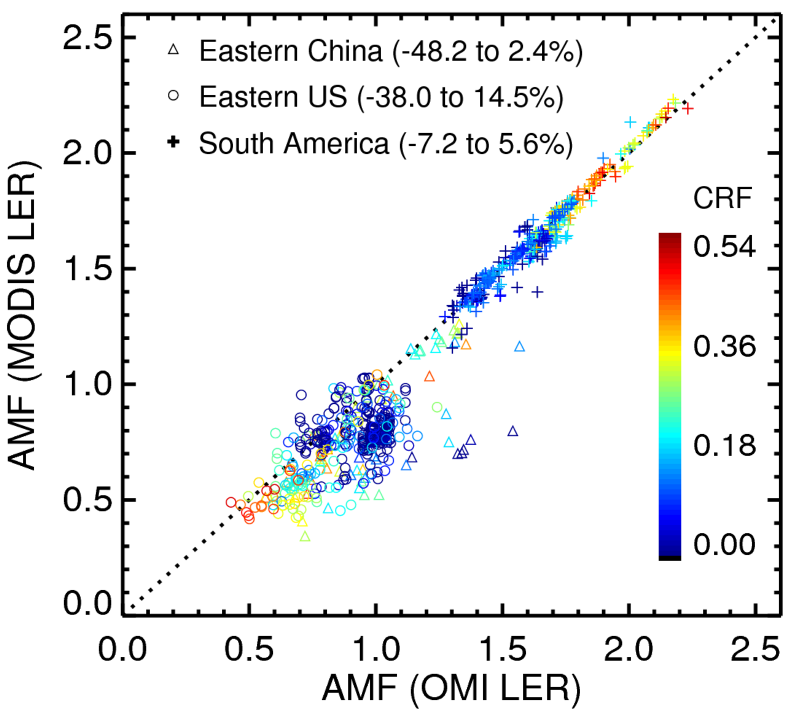

Fig. 13. AMFs calculated with geometry-dependent MODIS-based LERs and climatological OMI-based LERs over 5°x5° boxes in eastern China (115°–120°E, 36°–41°N, triangle), eastern US (75°–80°W, 36°–41°N, circle), and South America (55°–60°W, 20°–25°S, plus sign) for clear to moderately-cloud skies $f_r < 0.5$. AMF calculated with the MODIS-based LER includes the combined effects of surface BRDF and O_2-O_2 cloud parameters. Symbols are color-coded by f_r. Numbers in parentheses represent % differences at the 2nd and 98th percentile ranges.